

Heuristic machinery to uncover hidden features of $SU(N)$ Fermions with neural networks

Entong Zhao,¹ Jeongwon Lee,² Chengdong He,¹ Zejian Ren,¹ Elnur Hajiyev,¹ Junwei Liu,¹ and Gyu-Boong Jo¹

¹*Department of Physics, The Hong Kong University of Science and Technology,
Clear Water Bay, Kowloon, Hong Kong, China*

²*HKUST Jockey Club Institute of Advanced Study,
The Hong Kong University of Science and Technology,
Clear Water Bay, Kowloon, Hong Kong, China*

The power of machine learning (ML) provides the possibility of analyzing experimental measurements with an unprecedented sensitivity. However, it still remains challenging to uncover hidden features directly related to physical observables and to understand physics behind from ordinary experimental data using ML. Here, we introduce a heuristic machinery by combining the power of ML and the “trial and error” in a supervised way. We use our machinery to reveal hidden thermodynamic features in the density profile of ultracold fermions interacting within $SU(N)$ spin symmetry prepared in a quantum simulator, and discover their connection to spin multiplicity. Although such spin symmetry should manifest itself in a many-body wavefunction, it is elusive how the momentum distribution of fermions, the most ordinary measurement, reveals the effect of spin symmetry. Using a fully trained convolutional neural network (NN) with a remarkably high accuracy of $\sim 94\%$ for detection of the spin multiplicity, we investigate the dependency of accuracy on various hidden features with filtered measurements. Guided by our machinery, we verify how the NN extracts a thermodynamic compressibility from density fluctuations within the single image. Our machine learning framework shows a potential to validate theoretical descriptions of $SU(N)$ Fermi liquids, and to identify hidden features even for highly complex quantum matters with minimal prior understanding.

Multi-component fermions with $SU(N)$ -symmetric interactions holds a singular position as a prototype system for understanding quantum many-body phenomena in condensed matter physics, high energy physics and atomic physics [1]. In condensed matter, for example, interacting electrons usually possess $SU(2)$ symmetry, while there are emergent higher spin symmetry for the low-energy property of systems, as the $SU(4)$ symmetry in graphene due to the combination of spin and valley degree of freedom [2]. In quantum chromodynamics, nuclear interactions are represented by $SU(3)$ symmetry [3, 4]. In the past decades, developments in cooling and trapping of alkaline-earth-like (AEL) fermions [5] have opened new possibilities to achieve even higher spin symmetries owing to their distinctive inter-particle interactions, and thus provided ideal platforms to study various $SU(N)$ fermionic systems [1, 6, 7]. Although the role of $SU(N)$ symmetry has been probed in optical lattices [8–15], the comprehensive characterization of interacting $SU(N)$ fermions in bulk, wherein the $SU(N)$ Fermi liquid description is valid, has still remained challenging [16–19]. One of the bottlenecks is that many $SU(N)$ -dependent properties cannot directly be measured by the current experimental approaches and their connections to other measurements like density profiles still remain elusive. Developing new experimental techniques or designing new approaches to uncover the hidden connection of various spin-dependent properties with the available experimental measurements in $SU(N)$ interacting fermions is crucial to advance our understanding of $SU(N)$ symmetry and the corresponding many-body phenomena.

Here, we propose a general-purpose heuristic machin-

ery to uncover hidden thermodynamic features in ordinary experimental measurements of $SU(N)$ Fermi gas by combining philosophy of “trial and error” and the great power of machine learning techniques especially the convolutional neural network (NN) in uncovering hidden features of experimental images. This machinery consists of four parts: (1) Prepare the similar experiment measurements without the explicit features directly related to the physical observable; (2) Train the neural networks with the labelled measurements until realizing high accuracy; (3) Exploring the dependency of accuracy on various hidden features with filtered measurements; (4) Verify the dependency in theory and experiment.

To demonstrate the power of the proposed machinery concretely, we take the density profile of momentum distribution of a $SU(N)$ Fermi gas as an example to reveal its hidden features and use spin multiplicity as a physical observable to explore its connection to the hidden features. Based on this machinery, we demonstrate that one can extract important hidden features even in the most ordinary density profiles, and successfully reveal the strong dependence of spin multiplicity on both low-momentum fluctuations and high-momentum distribution, which enables a high accuracy $\sim 94\%$ for detecting the spin multiplicity in a single snapshot of density profile. To further verify the validity of the discovered connection between the hidden features and physical observable, we further measure the thermodynamic compressibility from density fluctuations within a single image benchmarking ML processes, which turns out to be in very good agreement with $SU(N)$ Fermi liquid descriptions. Besides providing general-purpose methods

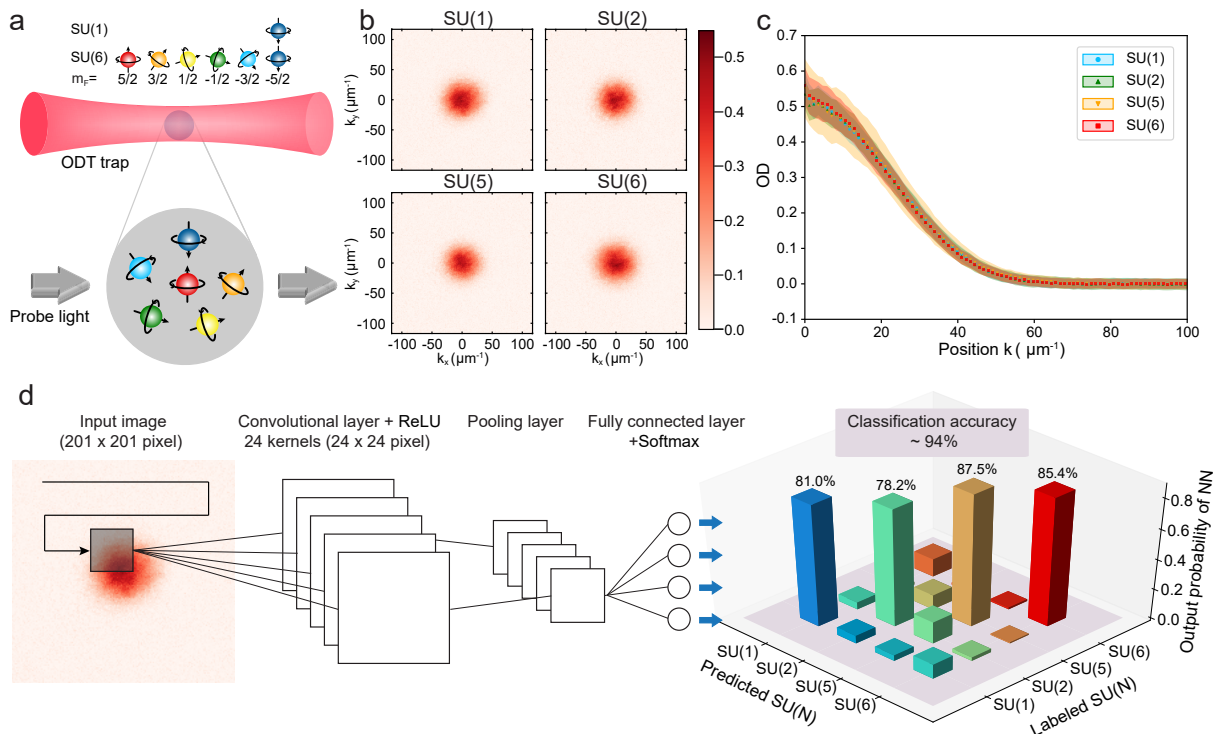


FIG. 1. **Distinguishing SU(N) fermions based on spin multiplicity by machine learning.** (a) Schematic of preparing SU(N) gases in the ODT. The momentum distribution of the SU(N) Fermi liquid of ^{173}Yb atoms with tunable spin configuration is recorded. The collected dataset are then fed into the NN as the input images for classification. (b) Examples of single experimental images of SU(N) gases. (c) Radial averaged OD profiles in different SU(N) gases. The shaded region represents the fluctuation of the density profile. (d) Experimental images of SU(N) gases are loaded into the neural network with one single convolutional layer. The white line and window represent how the kernel slides across the image. The output layer classifies the image into one of the class (i.e. SU(1), SU(2), SU(5), SU(6)) resulting in a classification accuracy around 94%. For each input image, NN outputs probabilities of different SU(N) with the highest value of the correct class. The output probabilities of NN is averaged over the validation dataset.

to uncover various hidden features and consolidate our understanding of SU(N) fermions, our approaches also complement recent ML studies of quantum many-body physics to explore the underlying physics [20–26].

TRAIN NEURAL NETWORKS TO CLASSIFY SU(N) FERMIONS

The first step of the proposed machinery is to prepare the experimental measurements labeled by the physical observable. Here, we choose one of the most ordinary experimental measurements for studying SU(N) Fermi gases, the density profile, and the spin multiplicity as the physical observable. In our experiment, a degenerate SU(N) Fermi gas as large as $N=6$ is prepared in an optical trap, and the density profile is recorded by taking spin-insensitive absorption images after time-of-flight expansion, yielding the momentum distribution (see Methods). In principle, the density profile contains the momentum-space information of SU(N) inter-

acting fermions that reflects various thermodynamic observables, which is the underlying reason for the success of using ML techniques to detect the spin multiplicity. However, the effect of spin multiplicity on the momentum distribution is extremely small compared to other observables such as the fugacity and the atom number because of small interaction strength. Therefore, to uncover hidden features related spin multiplicity, it is critical to prepare similar density profiles otherwise the NNs will directly use other quantities (e.g. fugacity or atom number) to do the classification. It motivates us to naturally propose one of the key points in our machinery (Fig. 1b,c), i.e., one needs to prepare featureless experimental measurements without explicitly known attributes directly related to the physical observable (i.e. spin multiplicity in our work).

In details, we focus on the density profiles with the interaction parameters $k_F a_s \simeq 0.3$ where k_F is the Fermi wave vector and a_s the scattering wavelength and only select the profiles based on similarities in widths of Gaussian fitting of the density profiles to result in indistinguishable momentum profiles as shown in Fig. 1b,c (see Methods). We collect 200 density profiles for each class

of SU(1), SU(2), SU(5), and SU(6) (Fig. 1b). We randomly feed 150 of them to train the NNs by implementing the supervised machine learning techniques with spin multiplicity as labels, and use the remaining 50 profiles to evaluate the classification accuracy. To maximize the accuracy of NNs, we choose the architecture of convolutional neural networks (CNNs) that are very suitable to explore the hidden features in an image (more details in Methods), as shown in Fig. 1d. By choosing the suitable structures and parameters in the CNNs, we can realize a very high accuracy $\sim 94\%$, which is much better than the random guess (25%). We also test various unsupervised learning techniques such as the typical principal component analysis [27, 28] and only can get a low classification accuracy of only $\sim 43\%$. Moreover, it is worth to emphasize that the remarkably high accuracy $\sim 94\%$ of NNs is achieved by using only a single snapshot of the density profiles. All these results indicate that there are indeed some hidden features in the density profile that determine the spin multiplicity and the well-trained NNs successfully capture the connections between these hidden features and the spin multiplicity, which is usually not detectable in a single snapshot in all the previous studies. The well-trained NNs are excellent starting point for the following steps of our machinery.

EXTRACT HIDDEN FEATURES IN LOW AND HIGH MOMENTUM PARTS

We now show how to analyze the attributes processed by the well-trained NNs and extract hidden features determining the spin multiplicity step by step. Due to the limited interpretation of NNs, it is usually very difficult to reveal the hidden features and the nonlinear dependency of physical observable on these hidden features. This comes to the third part of our machinery, we propose to reveal the hidden features and rules by studying the effect of deliberately filtered experimental images on classification accuracies.

The basic idea is to follow the philosophy of “trial and error” in order to examine which parts of the density profile are related to the spin multiplicity as described in Fig. 2a. Usually, it is more efficient to use some prior knowledge, which can be obtained in our limited understanding of the current system or the well-established understanding of the similar system. In our example of studying the interacting SU(N) fermions, we use the prior knowledge of non-interacting fermions and the associated energy (length) scale in choosing various filters in the momentum space. It is conceivable that our heuristic machinery can be applied to other systems.

To do this, we manually replace parts of the experimental images and then check the classification accuracy. Since different information is removed in different types of filtered images, the classification accuracy will decrease and the drop should be different, which will reveal what

kind of information is more important. As shown in Fig. 2b, we first use the Gaussian and Fermi-Dirac fitting profile to do the test based on the prior knowledge of non-interacting fermions. It turns out that the classification accuracy significantly decreases for both cases, and the accuracy drop of the Gaussian fitting profile is even more, which implies the machine learned profiles to be closer to the Fermi-Dirac type. We further test the variations in accuracies by replacing profiles with radially averaged profiles, which resulted in test accuracies even higher than the Fermi-Dirac fitting cases. However, the differences in accuracies between the radially averaged and Fermi-Dirac are much smaller compared to the differences between Fermi-Dirac and Gaussian, suggesting the SU(N) dependent modifications of the Fermi-Dirac distribution to be extremely small.

Moreover, compared to the binned case, the much larger decrease in all the three types of filters with various fitting functions directly implies that the high momentum parts are very important for determining the spin multiplicity since all of them completely remove the SU(N) dependent effect in the high momentum tail that reflects short-range interaction physics. This motivated us to independently evaluate the contributions of low and high momentum parts by classifying the masked images with the well-trained NN as shown in Fig. 3a and b. We choose two different types of masks for the region of the replacements, which will be referred as background and central masks, respectively. Background mask covers from the edge of the image to some atomic momentum k_c , while central mask covers from the center to k_c . Then we replace the region and re-evaluate the test accuracies of the pre-trained NN.

First, we set the cut-off momentum of $k_c=70 \mu m^{-1}$ such that $>99\%$ of atoms are contained within the low momentum region (Fig. 3a) that still allows us to classify the spin multiplicity with the accuracy of 88%. While this confirms that a NN perceive spin-dependent information in low momentum parts, questions remain on why the accuracies are not fully recovered beyond 94%. Such observation confirms the importance of the high momentum information. In Fig. 3b, we prepare a data set with a high momentum part only ($k > k_c=70 \mu m^{-1}$), in which a low momentum region is deliberately replaced by the same fake image. Surprisingly, the test classification accuracy is still $>50\%$, and the overall classification accuracy increases to 65% when a NN is re-trained. Such a high accuracy based on the few information of only $<1\%$ of atoms strongly implies that the high momentum tail is crucial for determining the spin multiplicity.

High momentum tails

In light of these results, we speculate that NNs utilize hidden features in the high momentum part. To confirm this, we check the dependence of classification accuracy with the fully trained NNs on each SU($N=1,2,5,6$) class, and we find the classification accuracy increases with N in Fig. 3b. In addition, the output probabil-

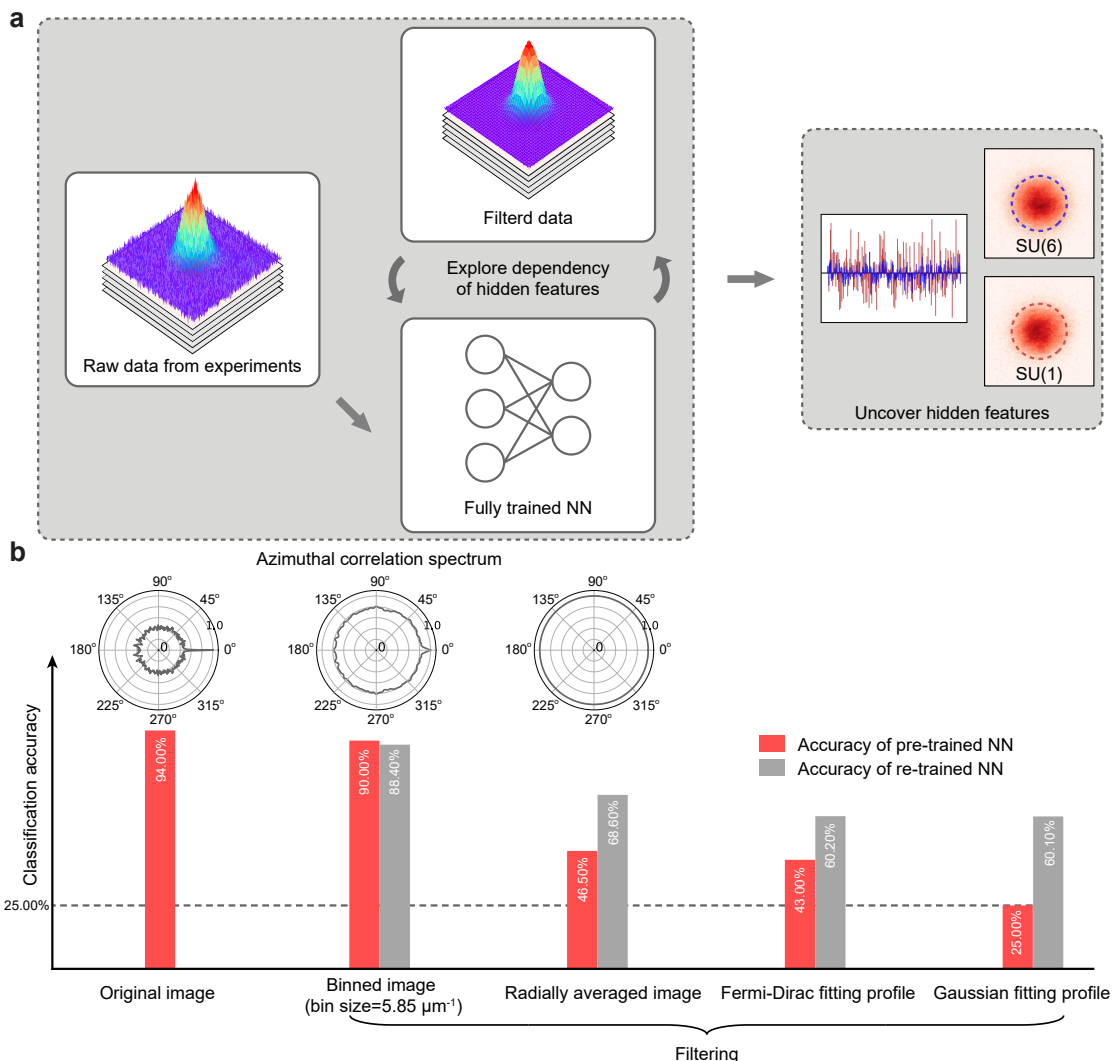


FIG. 2. **Revealing hidden features with NNs using deliberately filtered experimental images** (a) Our heuristic machinery to uncover hidden features. (b) Effect of image filtering on the classification accuracy by neural networks trained with original (red) and filtered (grey) experimental images. The retraining process follows the same procedure of original training with fixed neural network parameters and hyper-parameters (e.g. the number of epochs and learning rate). In the inset, the azimuthal correlation spectra calculated at $k = 58.5 \mu\text{m}^{-1}$ are shown.

ity of the correct spin multiplicity increases with N (see Fig. 3b). These results indicate that the hidden feature being used in NNs becomes more prominent with increasing spin multiplicity N , which is consistent with the fact that atom-atom interactions are absent in the case of SU(1) due to the Pauli principle in the ultracold regime while are significantly enhanced in SU(6) fermions. Indeed, the amount of short-range interactions should be revealed in the high momentum distribution in which the weight of such high momentum tail is determined by the central quantity, so-called the contact [29–31] in a dilute quantum gas. The contact governs many other physical observables [32, 33], and has been probed in strongly interacting gases [32–38] and even in a weakly interacting gas with SU(N) symmetric interactions [17]. It is conceivable that the NNs detect the high momentum distri-

bution within a single image in contrast to the previous work where hundreds of momentum-space images are statistically averaged in a ^{173}Yb gas [17]. To be noted, our observation is consistent with the direct measurement of the high momentum tail in the region of $k/k_F > 3$ [17], which is corresponding to $k > 100 \mu\text{m}^{-1}$ for an SU(1) gas in this work.

Evaluating detection accuracy with tunable masks

To reveal the hidden features in both low momentum and high momentum regions and build up the concrete connections between these hidden features and the spin multiplicity, we now quantitatively analyze the changes inflicted on the test accuracies when the cut-off momen-

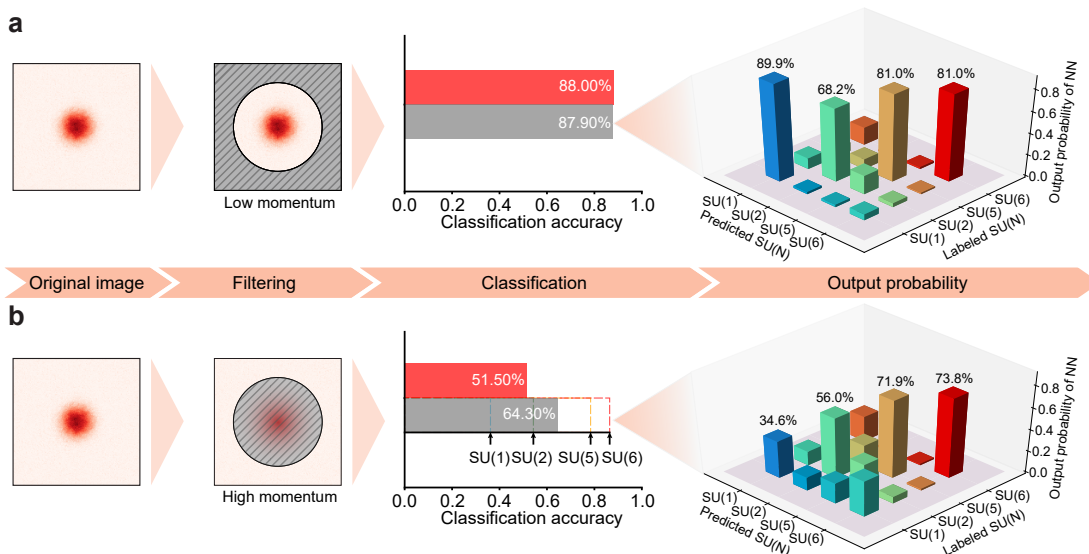


FIG. 3. **Hidden features in low and high momentum parts** Classification accuracy with neural networks trained only with low (a) and high (b) momentum parts. Retraining of the neural networks with only high or low momentum parts enhances the accuracy as shown in grey bars. For high momentum parts, classification accuracy increases with N as shown in black ticks in (b). For the re-training NN, the output probabilities of the NN are shown for input images.

tum k_c is tuned over. It is clearly shown in Fig. 4a that the test accuracies decrease to $\sim 25\%$ by complete replacements of the images by the same average image. This accuracy is gradually recovered up to almost 90% when k_c is increased to $k_c \simeq 70 \mu\text{m}^{-1}$ being consistent with the result in Fig. 2, as less information from the low momentum regime is removed. Based on replacement analysis, it is conceivable that $SU(N)$ dependent features must exist in the low momentum part as we will discuss details below. In comparison, the classification accuracy of the binned images (bin size = $5.85 \mu\text{m}^{-1}$) does not decrease too much, which is only a partial removal of fluctuations. As a complementary study, we utilize the central mask and replace the low momentum information up to variable momenta of k_c in Fig. 4b. The classification accuracy gradually decreases with increasing k_c from 0 to $\sim 50 \mu\text{m}^{-1}$ as the information within the density profile is increasingly removed. However, the classification accuracy stays over 50% around $k_c = 50 \sim 70 \mu\text{m}^{-1}$, which strongly suggests that the high momentum tails of the density distribution still contribute towards the classifications based on $SU(N)$. Beyond $k_c = 80 \mu\text{m}^{-1}$, where the atomic shot-noise becomes comparable to the background shot-noise level, the test accuracies rapidly drop for both cases.

Density fluctuations and compressibility

The question still remains as to what dominant feature classifies spin multiplicity in the low momentum regime. Considering the fact that the density profiles do not show discernible spin-dependent features (Fig. 1c), we specu-

late that the NNs utilize the correlation for classification. Based on the significant decrease of the accuracy with profiles being radially averaged in Fig. 2b, we investigate the azimuthal correlation spectrum showing a strong signal in the original and binned images while flattened at all angles for the radially averaged images. Therefore, we hypothesize the NNs detect density fluctuations along the azimuthal direction, therefore distinguishing $SU(N)$ dependent features.

To understand how the density fluctuations reveal spin multiplicity, we consider the fluctuation-dissipation theorem by which the thermodynamic compressibility $\kappa = \frac{1}{n^2} \frac{\partial n}{\partial \mu}$ can be measured through density fluctuations (i.e. atom number fluctuations) [19, 39–41] where n is the local density and μ the local chemical potential. For repulsively interacting $SU(N)$ fermions, it is known that the compressibility κ decreases with increasing spin multiplicity N as $(\kappa/\kappa_0)^{-1} = 1 + \frac{2}{\pi} (k_F a_s)(N-1)(1 + \epsilon k_F a_s)$ where κ_0 is the compressibility of an ideal Fermi gas and $\epsilon = \frac{2}{15\pi} (22 - 4 \ln 2)$ [42]. Here, the atom number fluctuations are further suppressed by the Pauli blocking in the degenerate regime showing sub-Poissonian fluctuations as $\sigma_{N_a}^2/\bar{N}_a \propto k_B T$ where N_a indicates the atom number measured in the small volume. Therefore, one finds the relative atom number fluctuation $\sigma_{N_a}^2/\bar{N}_a$ is given as

$$\sigma_{N_a}^2/\bar{N}_a = nk_B T \kappa = \frac{3}{2} \frac{T/T_F}{1 + \frac{2}{\pi} k_F a_s (N-1)(1 + \epsilon k_F a_s)}$$

In our experiment, an atomic sample ballistically expands from the harmonic trap preserving occupation statistics of the phase space during the expansion [43, 44].

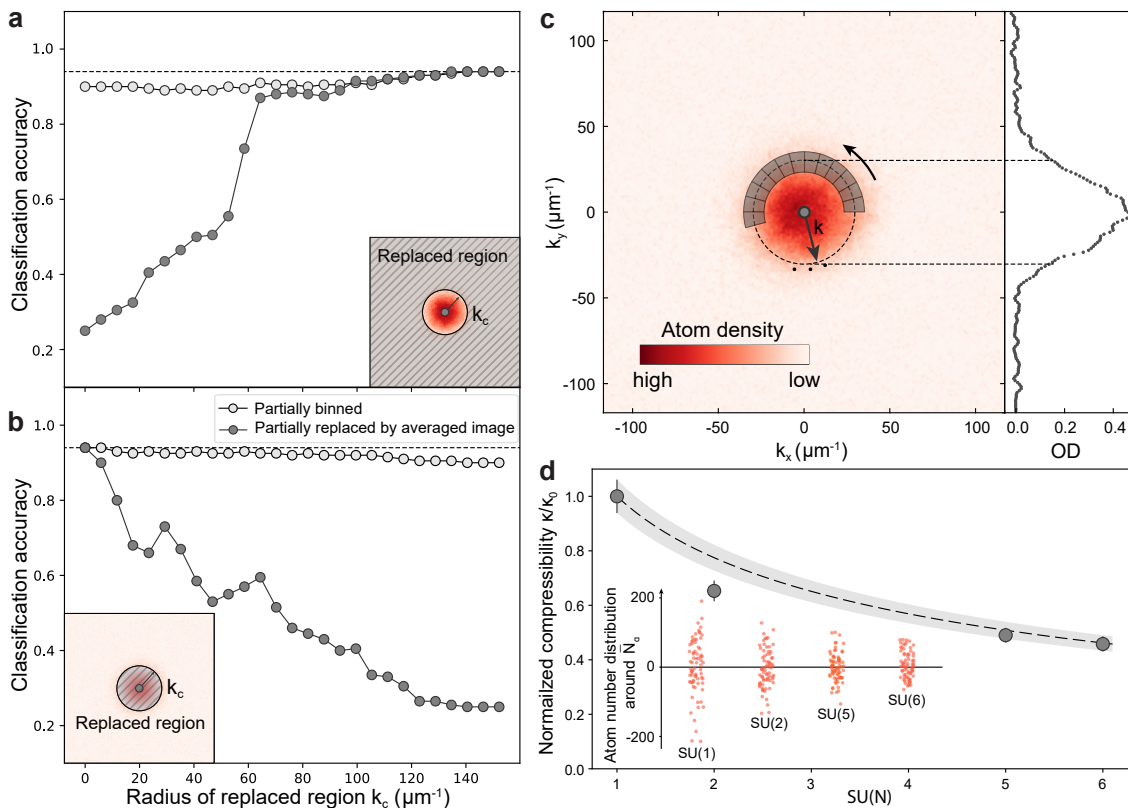


FIG. 4. **Verification of ML-aided detection : density fluctuations and thermodynamic compressibility** (a,b) Classification accuracy of the correct class as a function of the cutoff momentum k_c of the mask. The dotted line indicate the accuracy of 94 %. (c) Measurement of density fluctuations with a snapshot. In a line-of-sight integrated density profile, a series of bins containing on average \bar{N}_a atoms is chosen along the azimuthal direction. Each bin is about 10 (in azimuthal direction) by 17 (in radial direction) μm much larger than the optical resolution of the imaging system. The density profile at $k_x=0$ is shown. (d) The normalized compressibility of SU(N) fermions κ/κ_0 is measured by relative density fluctuations as $\kappa/\kappa_0 = \zeta_{SU(N)}/\zeta_{SU(1)}$. The error bar shows the standard error. The dashed line indicates the theory curve $\kappa/\kappa_0 = [1 + \frac{2}{\pi} k_F a_s (N-1)(1 + \epsilon k_F a_s)]^{-1}$ with the uncertainty represented by the shaded region considering the standard error of $\zeta_{SU(1)}$. The inset shows the distribution of the atom number per bin around the average, $(N - \bar{N}_a)/(T/T_F)$, normalized by the degenerate temperature where \bar{N}_a is the average atom number.

Instead of repeatedly producing identical samples and monitoring a small region at the certain position [39], the relative atom number fluctuations can be extracted along the azimuthal bins containing the same number of atoms on average (therefore resulting in equivalent optical density) within a single image even though a grouping of ideally equivalent bins is challenging and the fluctuation measurement is susceptible to the systematic variations. Nevertheless, our analysis in the following suggests that the NN uses this information for distinguishing SU(N) fermions.

To verify this hidden feature, we choose a series of bins containing ~ 450 atoms on average in a line-of-sight integrated density profile along the azimuthal direction (Fig. 4c), and analyze statistics. To have a sufficiently large number of bins for statistical analysis, we perform the measurements at varying momenta on the ring with $(k_x^2 + k_y^2)^{1/2} \simeq 28 \mu\text{m}$ around the center of the distribution. Both the temperature and spin multiplic-

ity are known to affect the atomic density fluctuations through the change in compressibility. Therefore, we normalize relative atom fluctuations by the temperature as $\zeta_{SU(N)} = \frac{\sigma_{N_a}^2}{\bar{N}_a} / \frac{T}{T_F}$ to reveal SU(N) interaction effect from a single snapshot. In Fig. 4d, we then plot the statistical value of $\zeta_{SU(N)}/\zeta_{SU(1)}$. This measurement indeed reveals the normalized thermodynamic compressibility $\kappa/\kappa_0 = \zeta_{SU(N)}/\zeta_{SU(1)}$ showing the enhanced interaction $k_F a_s (N-1)$. The error bar indicates the standard error from 150 different density profiles. Whereas the scaling of the measured density fluctuation with N is in good agreement with theoretical prediction, experimental results for SU($N > 1$) lie systematically below theoretical ones. The discrepancy may be due to interactions that remain finite during the expansion, which could slightly perturb the occupation statistics of the phase space.

DISCUSSION AND CONCLUSION

To scrutinize the effects of $SU(N)$ symmetric interactions, we have provided the NN with altered images and probed specific attributes of the profiles independently. We found that the high momentum tail and density fluctuation information significantly contribute to the $SU(N)$ classification process. First of all, the high momentum tail of atomic density distributions are expected to exhibit Tan's contact, which encapsulates the many body interactions through set of universal relations. While the previous work required averaging of hundreds of images for the detection of the $SU(N)$ dependent contact [17], the NN's ability to determine the $SU(N)$ class with a single image provides an extremely efficient alternative route. However, the exact mechanism behind how the trained network collects the required information for extraction of the contact, whether it is through superior noise suppression or signal enhancement, is not known and left for future work.

The second dominant feature for the $SU(N)$ classification is the density fluctuation within the profile. Both the temperature and spin-multiplicity are known to affect the atomic density fluctuations through the change in compressibility. Sub-Poissonian density distributions have been observed in degenerate Fermi gases of atoms [39, 40] and molecules [41], where multiple images were used to obtain the statistics. For a single image, there exists multiple sets of density fluctuation measurements at vary-

ing momentums, where each measurements form a ring around the center of the distribution. Considering the decreased $SU(N)$ classification accuracy from the radially averaged data sets, the fluctuation information might have been utilized in addition to the contact to reflect the effects of compressibility. Lastly, we found that the low energy part of the density profile does not exhibit a signature as strong as the previous two features. While there has been a report of $SU(N)$ dependent modifications to the density distribution limited to the 1D case [16], the corresponding beyond mean-field effects in 3D remains challenging to be measured experimentally.

In conclusion, we have demonstrated the capabilities of the proposed machinery by classifying $SU(N)$ Fermi gases with their time-of-flight density distributions. The neural network provides classifications with an accuracy well beyond the conventional methods such as PCA. By applying different types of manipulations, we also find that the neural network combine the features from a high momentum signal and density fluctuations together to distinguish $SU(N)$. Future directions include predictions of T/T_F of $SU(N)$ Fermi gases based on regression algorithms, and explorations of human feedbacks to the machine learning process for feature extractions. Feature extraction through machine learning may facilitate research in many-body quantum systems, especially when there are excess of information from the measurements beyond our understandings.

-
- [1] M. A. Cazalilla and A. M. Rey, *Reports on Progress in Physics* **77**, 124401 (2014).
- [2] A. H. Castro Neto, F. Guinea, N. M. R. Peres, K. S. Novoselov and A. K. Geim, *Reviews of Modern Physics* **81**, 109 (2009).
- [3] M. Gell-Mann, *Physical Review* **125**, 1067 (1962).
- [4] Y. Ne'eman, *Nuclear Physics* **26**, 222 (1961).
- [5] C. He, E. Hājijev, Z. Ren, B. Song and G.-B. Jo, *Journal of Physics B: Atomic, Molecular and Optical Physics* **52**, 102001 (2019).
- [6] M. A. Cazalilla, A. F. Ho and M. Ueda, *New Journal of Physics* **52**, (2009).
- [7] R. Zhang, Y. Cheng, P. Zhang and H. Zhai, *Nature Reviews Physics* **2**, 213 (2020).
- [8] A. V. Gorshkov, M. Hermele, V. Gurarie, C. Xu, P. S. Julienne, J. Ye, P. Zoller, E. Demler, M. D. Lukin and A. M. Rey, *Nature Physics* **6**, 289 (2010).
- [9] S. Taie, R. Yamazaki, S. Sugawa and Y. Takahashi, *Nat. Phys.* **8**, 825 (2012).
- [10] X. Zhang, M. Bishof, S. L. Bromley, C. V. Kraus, M. S. Safronova, P. Zoller, A. M. Rey and J. Ye, *Science* **345**, 1467 (2014).
- [11] G. Cappellini, M. Mancini, G. Pagano, P. Lombardi, L. Livi, M. Siciliani De Cumis, P. Cancio, M. Pizzocaro, D. Calonico, F. Levi et al., *Physical Review Letters* **113**, 120402 (2014).
- [12] F. Scazza, C. Hofrichter, M. Höfer, P. C. De Groot, I. Bloch and S. Fölling, *Nature Physics* **10**, 779 (2014).
- [13] C. Hofrichter, L. Riegger, F. Scazza, M. Höfer, D. R. Fernandes, I. Bloch and S. Fölling, *Physical Review X* **6**, 021030 (2016).
- [14] H. Ozawa, S. Taie, Y. Takasu and Y. Takahashi, *Physical Review Letters* **121**, 225303 (2018).
- [15] A. Goban, R. B. Hutson, G. E. Marti, S. L. Campbell, M. A. Perlin, P. S. Julienne, J. P. D'Incao, A. M. Rey and J. Ye, *Nature* **563**, 369 (2018).
- [16] G. Pagano, M. Mancini, G. Cappellini, P. Lombardi, F. Schäfer, H. Hu, X.-J. Liu, J. Catani, C. Sias, M. Inguscio et al., *Nature Physics* **10**, 198 (2014).
- [17] B. Song, Y. Yan, C. He, Z. Ren, Q. Zhou and G.-B. Jo, *arXiv:1912.12105*, (2019).
- [18] C. He, Z. Ren, B. Song, E. Zhao, J. Lee, Y.-C. Zhang, S. Zhang and G.-B. Jo, *Physical Review Research* **2**, 012028(R) (2020).
- [19] L. Sonderhouse, C. Sanner, R. B. Hutson, A. Goban, T. Bilitewski, L. Yan, W. R. Milner, A. M. Rey and J. Ye, *arXiv:2003.02408v2*, (2020).
- [20] G. Carleo and M. Troyer, *Science* **355**, 602 (2017).
- [21] J. Carrasquilla and R. G. Melko, *Nature Physics* **13**, 431 (2017).
- [22] D.-L. Deng, X. Li and S. Das Sarma, *Physical Review X* **7**, 021021 (2017).
- [23] Y. Zhang, A. Mesaros, K. Fujita, S. D. Edkins, M. H. Hamidian, K. Ch'ng, H. Eisaki, S. Uchida, J. C. S. Davis, E. Khatami et al., *Nature* **570**, 484 (2019).
- [24] B. S. Rem, N. Käming, M. Tarnowski, L. Asteria, N.

- Fläschner, C. Becker, K. Sengstock and C. Weitenberg, *Nature Physics* **15**, 917 (2019).
- [25] L. Feng, J. Hu, L. W. Clark and C. Chin, *Science* **363**, 521 (2019).
- [26] A. Bohrdt, C. S. Chiu, G. Ji, M. Xu, D. Greif, M. Greiner, E. Demler, F. Grusdt and M. Knap, *Nature Physics* **363**, (2019).
- [27] Pearson K. *Phil. Mag.* **2**, 559-572. (1901).
- [28] Jackson JE. A user's guide to principal components. New York, Wiley. (1991).
- [29] S. Tan, *Annals of Physics* **323**, 2952 (2008).
- [30] S. Tan, *Annals of Physics* **323**, 2971 (2008).
- [31] S. Tan, *Annals of Physics* **323**, 2987 (2008).
- [32] J. T. Stewart, J. P. Gaebler, T. E. Drake and D. S. Jin, *Physical Review Letters* **104**, 235301 (2010).
- [33] E. D. Kuhnle, H. Hu, X. J. Liu, P. Dyke, M. Mark, P. D. Drummond, P. Hannaford and C. Vale, *Physical Review Letters* **105**, 070402 (2010).
- [34] G. B. Partridge, K. E. Strecker, R. I. Kamar, M. W. Jack and R. G. Hulet, *Physical Review Letters* **95**, 020404 (2005).
- [35] R. J. Fletcher, R. Lopes, J. Man, N. Navon, R. P. Smith, M. W. Zwierlein and Z. Hadzibabic, *Science* **355**, 377 (2017).
- [36] S. Laurent, M. Pierce, M. Delehay, T. Yefsah, F. Chevy and C. Salomon, *Physical Review Letters* **118**, (2017).
- [37] Z. Yu, J. H. Thywissen and S. Zhang, *Physical Review Letters* **115**, 135304 (2015).
- [38] C. Luciuk, S. Trotzky, S. Smale, Z. Yu, S. Zhang and J. H. Thywissen, *Nature Physics* **12**, 599 (2016).
- [39] C. Sanner, E. J. Su, A. Keshet, R. Gommers, Y.-i. Shin, W. Huang and W. Ketterle, *Physical Review Letters* **105**, 040401 (2010).
- [40] T. Mueller, B. Zimmermann, J. Meineke, J.-P. Brantut, T. Esslinger and H. Moritz, *Physical Review Letters* **105**, (2010).
- [41] W. G. Tobias, K. Matsuda, G. Valtolina, L. De Marco, J.-R. Li and J. Ye, *Physical review letters* **124**, 033401 (2020).
- [42] S. K. Yip, B.-L. Huang and J.-S. Kao, *Physical Review A* **89**, 920 (2014).
- [43] G. M. Bruun and C. W. Clark, *Physical Review A* **61**, 4 (2000).
- [44] S. Gupta, Z. Hadzibabic, J. Anglin and W. Ketterle, *Physical Review Letters* **92**, (2004).
- [45] B. Song, C. He, S. Zhang, E. Hajiyev, W. Huang, X.-J. Liu and G.-B. Jo, *Physical Review A* **94**, 061604 (2016).
- [46] B. Song, C. He, Z. Ren, E. Zhao, J. Lee and G.-B. Jo, *arXiv:2002.10053*, (2020).
- [47] Martn Abadi et al., *TensorFlow: Large-scale machine learning on heterogeneous systems*, Software available from tensorflow.org (2015).
- [48] F. Pedregosa et al., *Journal of Machine Learning Research* **12**, 2825 (2011).

ACKNOWLEDGMENTS We thank Tin-Lun Ho for helpful discussion. G.-B.J. acknowledges supports from the RGC and the Croucher Foundation through 16311516, 16305317, 16304918, 16306119, C6005-17G and N-HKUST601/17. This work is partially supported by the Innovative Exploratory Grant at HKUST. J.L. acknowledges supports from the RGC (N-HKUST626/18, 26302118 and 16305019).

* Correspondence and requests for materials should be addressed to G.-B.Jo (gbjo@ust.hk).

Supplementary Information

Sample preparation We prepare a balanced ultracold Fermi gas of ^{173}Yb atoms with $\text{SU}(N)$ symmetric interactions as large as $N=6$. (shown in Fig.1a). We begin by loading a laser cooled six-component Fermi gas, where the nuclear spin states are equally populated, into a three-dimensional optical dipole trap (ODT). The atoms are further evaporatively cooled in the ODT to a temperature range of 0.2 to 1.0 T/T_F , where T_F is the Fermi temperature. During the evaporation, different spin configurations are prepared via an optical pumping process using a narrow line-width transition of $^1S_0(F=5/2) \rightarrow ^3P_1(F'=7/2)$ at a wavelength of $\lambda = 556$ nmd. The σ^\pm -polarized pumping light removes unwanted m_F states of the ground manifold of 1S_0 [45] and produces a Fermi gas with tunable $\text{SU}(N)$ interactions, as the nuclear spin relaxation rates are negligible in our experiment. After the evaporative cooling, the ODT trap is further ramped up in 60 ms to obtain large enough trap frequencies $(\omega_x, \omega_y, \omega_z) = 2\pi \times (1400, 750, 250)$ Hz before 4 ms of time-of-flight expansion. We measure the density distributions by taking absorption images using a spin-insensitive $^1S_0(F=5/2) \rightarrow ^1P_1(F'=7/2)$ transition at 399 nm. The images are taken in random order with respect to their spin configurations, to avoid the possibility of a classification based on fluctuations in the background.

Data preparation All snapshots are first preprocessed by the fringe removal algorithm reported in Ref. [46]. Then cropped images are loaded into the neural network for further classification. For $\text{SU}(N)$ data, it is natural to prepare the same number of atoms per spin at constant T/T_F , in which case the normalized density profile is the same for different $\text{SU}(N)$. However, we find that the diffraction of the imaging light induces fringe patterns that depend on the total atom number in the experiment. Moreover, we inevitably change the level of background noise when we normalize the image by the total atom number. Therefore, we should keep the total atom number unchanged otherwise the neural network uses the background fringe pattern to classify the $\text{SU}(N)$ data. In our experiment, we post-select the data by using a Gaussian fitting to extract 200 images per each $\text{SU}(N)$ class, which allows us to obtain samples with similar profiles but different T/T_F . If we have kept different $\text{SU}(N)$ gases at constant T/T_F , the profiles are identical in the unit of k_F , instead of in the unit of pixel. Finally, 75 percent of the data was used for training and the remaining was for validation.

Neural network architecture and training proce-

dure The convolutional neural network (NN) is realized by using the Tensorflow in Python [47]. It is found that the result is not qualitatively sensitive to the choice of architecture such as the number of layers or the kernel size. Therefore, we remove superfluous layers to simplify our model. To train the network on the data with different spin configurations, we use learning rate of 0.0001 and the training epochs to be limited until the classification accuracy reaches the desired value. When the training and validation accuracies are significantly mis-matched (also known as the over-fitting issue), we stop the training process and re-train the network. After full training, the trained model is further used to test the filtered data.

We characterize the performance of trained NNs by obtaining the overall classification accuracy. As a complementary analysis of NNs, we also evaluate an output probability matrix that hints how the NNs perform among different classes. For one single image loaded into the NNs, for example, four probabilities are given and each of them represents how likely this image belongs to one specific class. In a probability matrix, every element A_{ij} represents the probability averaged over the results for all images with the true label j and predicted class i . The probability matrix A_{ij} is given in Fig. 3. Alternatively, we may also use the confusion matrix to represent the classification result, in which the element A_{ij} represents the number of samples classified into the class i with true label j . The result shows similar tendency with the probability matrix.

Feature extraction with principle component analysis. Another common machine learning technique is the principle component analysis (PCA). The PCA method is a widely used for extracting features of the data. It first converts a set of possibly correlated variables into a set of values of linearly uncorrelated variables, so-called principal components, through a linear transformation of the original coordinates. We use the PCA analysis as a starting point of unsupervised machine learning. The first few principle components usually contain most of the information, which makes PCA a very

efficient tool for dimensional reduction. After extracting the leading principle components, a cluster algorithm will be followed to further classify these dimensional reductive data.

Here, we use the KMeans cluster technique [48], which is a common technique used in unsupervised classification tasks. By continuous iteration, KMeans finds the center of different clusters and divide the data into new clusters according to the distance from the center. From the result of the KMeans cluster after the PCA analysis, overall classification accuracy is around 43.5 %. The accuracy is obtained by finding the correspondence with the best match. Even if we increase the number of principle component we use, the accuracy of the unsupervised case still maintains around 43 %. Alternatively, we may use PCA as the starting point of a supervised machine learning by choosing a KNN (k-nearest-neighbour) algorithm or SVM (support vector machine) as a classifier [48] The result is better than unsupervised case, but still not as powerful as neural network.

Data analysis In Fig.2a, we calculate the azimuthal correlation spectrum at $k = 58.5\mu m^{-1}$, which is defined as $C_k(\theta_j) = \frac{\sum_i [P_k(\theta_i)P_k(\theta_{i+j})]}{\sum_i P_k^2(\theta_i)}$, where $P_k(\theta_i)$ represents the optical density for a specific pixel at $k \sim 58.5\mu m^{-1}$ and angle $\sim \theta_i$. The formula can be further derived from the Fourier transform \mathcal{F} as $G = \frac{\mathcal{F}^{-1}(|\mathcal{F}(P_k)|^2)}{|P_k|^2}$. The azimuthal correlation spectrum shows how the image looks like its own copy after rotating a specific angle. For a radially averaged image, the correlation becomes 1 at any angle indicating no density fluctuations. When the image is binned, densities are only locally averaged resulting azimuthal correlation at nonzero angle less than 1.

Fig.4d shows density fluctuations measured along azimuthal bins containing the same number of atoms within a single image. Total 24 bins are chosen at the distance of $22 \sim 34\mu m^{-1}$ from the center of the cloud. Redundant pixels are removed at the border to keep all bins have the same number of pixels. The size of each bin is much larger than the optical resolution of the imaging system.